



## Fast micron-scale 3D printing with a resonant-scanning two-photon microscope



Benjamin W. Pearre<sup>a,\*</sup>, Christos Michas<sup>b</sup>, Jean-Marc Tsang<sup>b</sup>, Timothy J. Gardner<sup>a,b,1</sup>, Timothy M. Otchy<sup>a,1</sup>

<sup>a</sup> Department of Biology, Boston University, Boston, MA 02215, USA

<sup>b</sup> Department of Biomedical Engineering, Boston University, Boston, MA 02215, USA

### ARTICLE INFO

#### Keywords:

3D printing  
Additive manufacturing  
Lithography  
Direct laser writing  
Two-photon microscopy  
Resonant scanning

### ABSTRACT

3D printing allows rapid fabrication of complex objects from digital designs. One 3D-printing process, direct laser writing, polymerises a light-sensitive material by steering a focused laser beam through the shape of the object to be created. The highest-resolution direct laser writing systems use a femtosecond laser, steered using mechanised stages or galvanometer-controlled mirrors, to effect two-photon polymerisation. Here we report a new high-resolution direct laser writing system that employs a resonant mirror scanner to achieve a significant increase in printing speed over current methods while maintaining resolution on the order of a micron. This printer is based on a software modification to a commercially available resonant-scanning two-photon microscope. We demonstrate the complete process chain from hardware configuration and control software to the printing of objects of approximately  $400 \times 400 \times 350 \mu\text{m}$ , and validate performance with objective benchmarks. Released under an open-source license, this work makes micron-scale 3D printing available at little or no cost to the large community of two-photon microscope users, and paves the way toward widespread availability of precision-printed devices.

### 1. Introduction

Direct laser writing (DLW) lithography [1] is a 3D-printing technology that can be used to fabricate small-scale objects with complex geometries by programmatically exposing a light-sensitive material to a focused laser beam [2–6]. Using femtosecond laser pulses and two-photon polymerisation processes to write a solid object structure into a photoresist, DLW enables on-demand fabrication of complex 3D objects with micron-scale features [5,7–15]. While DLW achieves diffraction-limited resolution, the printing speed of DLW is slow, practically limiting the size of printed objects to cubic millimetres. The slowest DLW printers use stepper motors or piezoelectric stages, at speeds ranging from  $\sim 0.1$ – $30 \text{ mm/s}$  [16,17]. Printers controlling focal position with digital micromirror devices [18] or galvanometers [15,19–22] can increase the laser scan rate to tens or hundreds of  $\text{mm/s}$ . Indeed, recent reports include raster-scan printing with high-speed galvanometers that achieve up to  $400 \text{ mm/s}$  by operating the scan mirror near its resonant frequency [23]. Here we introduce the use of a commercial resonant imaging mirror operating at  $8 \text{ kHz}$ , which allows printing at speeds up to  $\sim 8000 \text{ mm/s}$ .

To increase not only the speed of this technology but also its availability and flexibility, the raster-scanning DLW (rDLW) system that we introduce is built on a standard resonant-scanning two-photon microscope and open-source control software that are common equipment in many physical and life science laboratories. Open design and standard commercial components offer easy modification and adaptation to accommodate new materials, object sizes, and techniques.

We demonstrate the capabilities of our resonant rDLW printer in the rapid fabrication of micron-scale objects. The instantiation reported here is capable of printing objects up to  $\sim 400 \times 400 \times 350 \mu\text{m}$  with minimum feature sizes of  $\sim 4 \times 1 \times 2 \mu\text{m}$  ( $X$ ,  $Y$ , and  $Z$ , respectively), with finer  $X$ -axis features available through the use of the microscope's zoom. Larger objects may be constructed by stitching together overlapping pieces of this size, although a discussion of stitching is beyond the scope of this work. We show that the use of a resonant scanner allows our system to print an object of this size and arbitrary geometric complexity in about  $20 \text{ s}$ —faster by an order of magnitude than the fastest systems previously available. We evaluate performance with objective metrics assessed using IP-Dip (Nanoscribe, GmbH), a proprietary refraction-index-matched resist developed for rapid, high-

\* Corresponding author.

E-mail address: [bwpearre@bu.edu](mailto:bwpearre@bu.edu) (B.W. Pearre).

<sup>1</sup> These authors contributed equally to this work.

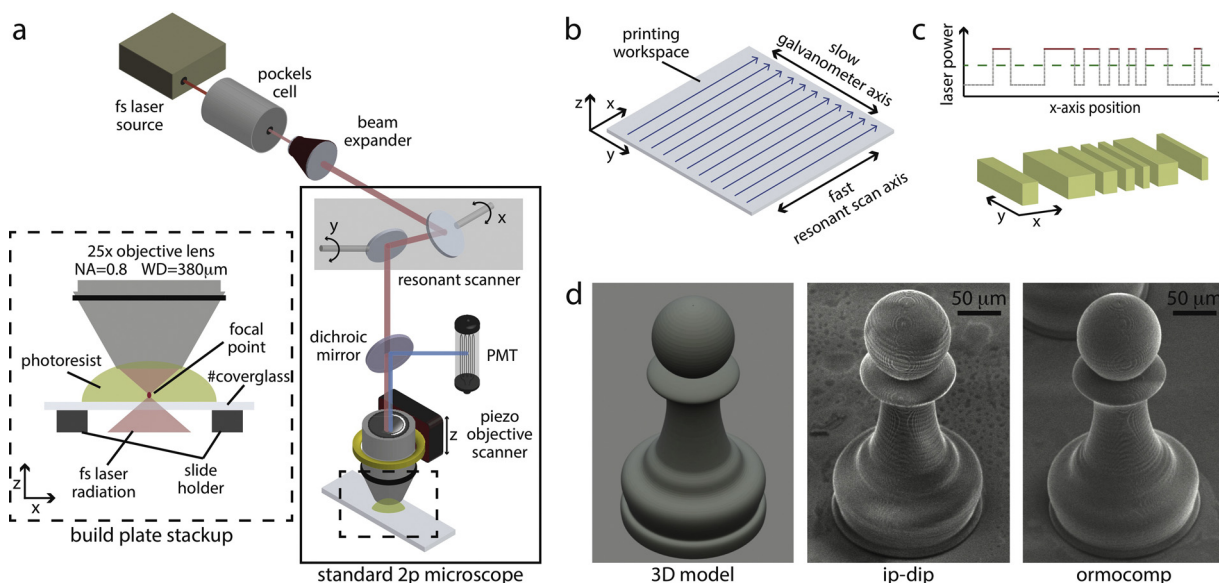


**Fig. 1.** Overview of the resonant rDLW printer. (a) Schematic of the optical path from laser source to printed object. Solid-outline box shows components comprising a standard resonant-scanning 2-photon microscope. Dash-outline box shows zoomed view of build plate stack. (b) The raster scanner rapidly sweeps the laser focus across the X-axis of the printing workspace; a slower galvanometer scans the laser focus across the Y-axis. (c) Top: laser power is modulated above (red line) and below (grey dotted line) the polymerisation threshold (green dashed line) throughout the X-axis sweep. Bottom: by applying this pattern of laser modulation over the workspace, solid features can be built up line by line and layer by layer. (d) Left: 3D model of a chess pawn. Center and Right: SEM micrograph of the chess pawn ( $192 \times 350 \mu\text{m}$ ) printed in IP-Dip photoresist (center) and Ormocomp (right) with our rDLW printer. (For interpretation of the references to colour in this figure legend, the reader is referred to the web version of this article.)

resolution DLW. In addition, we demonstrate the ability to print with a commercial polymer photoresist, Ormocomp. Finally, we release our application software under an open-source license. Taken together, this work provides a new approach for high-speed DLW and makes high-resolution direct laser writing more accessible to the existing community of two-photon microscope users.

## 2. Material and methods

The rDLW system we report fabricates objects by raster-scanning the focal point of a femtosecond laser through a volume of photoresist, defining the object structure line by line. The device schematic in Fig. 1a depicts the hardware configuration tested and reported here—essentially, a standard two-photon microscope with a resonant raster scanner and high-speed/high-extinction-ratio laser power modulator. This schematic need not be taken as prescriptive, as one of the benefits to having an open system is the ability to modify components to meet the requirements of new applications.

Throughout the manuscript, we use Cartesian coordinates to refer to directions and dimensions in the build envelope. Following this nomenclature, X and Y are the perpendicular axes spanning a single focal plane of the orthogonal Z direction. The microscope's zoom setting determines the size of this X–Y plane, which we refer to as the “workspace”. In keeping with this, X denotes the direction of the high-speed (7.91 kHz) raster scanner's sweeps, and Y identifies the slow galvanometer-controlled row index (Fig. 1b).

### 2.1. A 3D printer built on a two-photon microscope

The printer is built around a commercial two-photon microscope platform (Sutter Moveable Objective Microscope). A resonant + galvanometer scan module (Sutter MDR-R; 5-mm scan mirror) controls the laser's X–Y focal point within the build envelope. An immersion objective lens (25× magnification; numerical aperture (NA) of 0.8) with a refraction compensation ring (Zeiss LCI Plan-Neofluar; Model 420852-9972) was used for both printing and imaging. A piezo-scanner (Thorlabs PFM450) enabled fast, precise Z-axis

positioning of the objective lens (and hence the focal plane) during printing. The build plate is #0 coverglass (Goldseal 260320) supported at its edges by a slide holder (Thorlabs MAX3SLH), facilitating easy exchange of build plates and allowing the coverglass to break without damaging the objective in an accidental crash. A photomultiplier camera (Hamamatsu C8137-02) allowed imaging of the workspace and printed objects.

A tunable Ti–Sapphire laser system (Spectra-Physics Millennia Xs pump laser with Tsunami 3955 cavity) ( $\sim 120$  fs pulse duration, 80 MHz repetition) provided the laser radiation for both polymerisation and visualisation of the photoresist and printed objects. We used pump laser powers in the range of 6–10 W, resulting in a  $\sim 600$ –1400-mW mode-locked output beam at the polymerisation half-energy wavelength (tunable, but typically 780 nm). Beam intensity was modulated by a Pockels cell (ConOptics 350-80 cell and 302RM voltage amplifier) interfaced with a 3.33-MHz DAC (National Instruments PXIe-6356) (we note that this Pockels cell and driver are not rated for 3-MHz use, but the nonlinearity of the polymerisation reaction allows us to control printing voxelisation at a frequency higher than that for which the Pockels cell is rated. Nonetheless, we recommend that users work with a faster Pockels cell and driver in order to improve small-feature accuracy). Laser intensity was continuously monitored by sampling the passing beam (Thorlabs BSF10-B, SM05PD2A, and PDA200C). To flatten the profile and improve collimation, the beam was routed through a  $2 \times$  Galilean beam expander (Thorlabs GBE02-B) before entering the microscopy optics (Fig. 1a).

All components were interfaced with the control computer via a dedicated data acquisition system (National Instruments PXIe-1073 chassis with PXIe-6356 and PXIe-6341 cards). An air-shock isolation table (Newport ST Table and I-2000 Isolators) minimised vibration due to floor movements.

### 2.2. PrintImage: a resonant-rDLW control application

Because the printer is built on a two-photon microscope, we chose to use a popular open-source microscopy software package, ScanImage (Vidrio Technologies) [24], as the basis for system control. To

implement printer functionality, we developed a custom MATLAB application, PrintImage, that runs alongside ScanImage to control print object voxelisation, calculate the laser power modulation sequence, and manage the printing-specific parts of the imaging process.

Print objects may be designed using any computer-aided-design or engineering (CAD/CAE) software capable of exporting Stereolithography (STL) files. STL files, which define the unstructured triangulated surface of the object by the unit normal and vertices of the triangles using a 3D Cartesian coordinate system, are transformed into a “watertight” solid object of specific dimensions that is mapped onto the predefined set of printer positions via a mesh voxelisation routine. Voxel  $Y$  and  $Z$  positions are determined by the number of scan lines and vertical slices specified by the user;  $X$  positions are computed as described in Section 2.4.1.

Once the object is voxelised, the series of filled and empty voxels along the  $X$  direction of each  $Y$  row (blue arrows, Fig. 1b) is converted into a vector of supra- and sub-polymerisation-threshold laser powers (Fig. 1c) that defines the geometry (for each  $Y$  row) of the printed object. Repeating this translation for each  $Y$  row in every  $Z$  plane, the required laser power at every point within the build envelope is computed before the volume print scan is initiated. Power correction factors are applied to compensate for variable beam speed, spherical aberrations in the objective lens, or other nonuniformities (see Section 2.5). During printing, ScanImage executes a volume scan (as is typically performed for volumetric two-photon calcium imaging) using the laser power sequence precomputed by PrintImage (Fig. 1c), thus creating the printed object (Fig. 1d).

### 2.3. Calibration and accuracy

The dimensional accuracy of printed parts depends on the care with which the microscope is calibrated. Calibration is effected by adjusting ScanImage's optical workspace parameters, which are used as the basis for PrintImage's geometry computations. Because three different mechanisms control the laser focal point position in 3D space ( $X$  axis: resonant scanning mirror;  $Y$  axis: galvanometer mirror;  $Z$  axis: piezo objective scanner), it is necessary to tune the microscope's printing accuracy separately for each dimension.

For calibration and accuracy measurement of the  $X$ - $Y$  plane, we designed calibration cubes (Fig. 2b) and a ruler (Fig. 2c). Calibrating the  $Z$ -axis required a device that allowed measurement of focal-plane depth by imaging a printed part either in ScanImage or on other imaging systems, for which we developed the staircase ruler shown in Fig. 2d. To ensure the printed part securely adheres to the build plate, the focal plane is set at or slightly below the build plate surface. Since we currently do this manually, our printing process leads to variability (a few microns, depending on the user) in the starting height of the print. Therefore we measured  $Z$  accuracy by examining the height of each step of the staircase with respect to an arbitrary origin. Automatic detection of the build plate surface would improve consistency, and is left as future work.

These calibration objects were used to tune ScanImage's scaling parameters by two methods: (1) by using the rDLW printer to image objects of known size; and (2) by printing objects with the rDLW printer and measuring them using independently calibrated devices. While either method may be used for calibration, the latter was used for characterising printing accuracy.

In order to create objects of known dimensions, we used a commercial DLW printer to print rulers with IP-Dip photoresist (Fig. 2a; Section 2.7), and confirmed the dimensions of the rulers with SEM micrographs (Section 2.8) (when printed on the commercial DLW system, the 10- $\mu\text{m}$  ruler tics measured 9.93  $\mu\text{m}$  with a SEM two-pixel error  $\pm 0.25 \mu\text{m}$ ). We imaged these rulers with our rDLW printer and adjusted ScanImage's optical scaling parameters until the objects' sizes were correctly reported. If a calibrated DLW printer is not available, fluorescent rulers may be created [25].

When using our rDLW system to print the calibration objects, we measured the discrepancy between desired and actual object dimensions, and adjusted ScanImage's workspace size parameters to null the difference. Measurements were made using SEM micrographs (Section 2.8) for  $X$  and  $Y$ -axes, and an optical surface profiler (Zygo NewView 6300) for the  $Z$ -axis.

### 2.4. Resolution

#### 2.4.1. The resonant scanner

As the resonant scanner sweeps the laser's focal point back and forth across the  $X$ -axis of the printer's workspace, the beam moves through the photoresist with sinusoidally varying velocity (Fig. 3a). If the centre of the sweep is defined as  $t = 0$ , the oscillation frequency as  $F_r$ , and the maximum beam excursion as  $\xi$ , then the focal point's position  $x$  at time  $t$  is given by  $x = \xi \sin(2\pi t F_r)$  (Fig. 3b, blue line). Beam velocity,  $\delta x / \delta t$ , rapidly approaches zero at the sweep extremes, so ScanImage restricts the usable portion of the raster scan to a central fraction,  $D$ , of the scan line, resulting in a printing workspace of width  $2\xi D$ . From the equation above, one sweep from  $-\xi$  to  $\xi$  will take time  $t = 1/(2F_r)$ , so the beam will traverse the subsection spanning  $D$  in  $t = 2 \arcsin(D)/(2\pi F_r)$ . If laser power (controlled by the Pockels cell) has a modulation frequency of  $F_p$ , then power can be updated every  $1/F_p$  seconds; this update rate enables  $r_x = 2F_p \arcsin(D)/(2\pi F_r)$  potential changes in laser power level (i.e., printing voxels) during a single  $X$ -axis scan. In our instantiation, the resonant scanner frequency ( $F_r \approx 8 \text{ kHz}$ ), the Pockels cell update rate ( $F_p \approx 3.33 \text{ MHz}$ ), and ScanImage's workspace restriction ( $D = 0.9$ ), result in a maximum of 152 print voxels along the  $X$ -axis.

Resonant-scanner-based control results in higher resolution near the edges of its sweep than in the centre, and allows higher resolution as workspace size decreases. For example, on our rDLW system, printing at  $1.3 \times$  zoom yields a  $512 \times 512\text{-}\mu\text{m}$   $X$ - $Y$  workspace. On the  $X$ -axis, voxels are spaced on average every  $V/r_x$  for a workspace of span  $V$ , so at this zoom our rDLW printer is expected to have a  $3.4\text{-}\mu\text{m}$  mean voxel size along the  $X$ -axis. At  $2.6 \times$  zoom, the mean voxel size along  $X$  is expected to be  $1.7 \mu\text{m}$  over the  $256 \times 256\text{-}\mu\text{m}$  workspace.

The use of a resonant scanner leads to significant variation about this mean, since laser power can be changed only at locations specified by the position function ( $\xi \sin(2\pi t F_r)$ ; Fig. 3b, black ticks) at a frequency equal to the laser power modulation rate,  $F_p$ . Thus, actual voxel size is nonuniform across the  $X$ -axis, with smaller voxels at the edges of the workspace than near the centre, proportional to  $\cos(\arcsin x)$  for  $x \in [-D\xi \dots D\xi]$  scaled and centred over  $V$ . As zoom level reduces workspace size  $V$ , expected voxel sizes over the  $X$ -axis decrease linearly until they become limited by optics or photon wavelength.

We treat the location of the centre of the focal point as the voxel location, since the degree to which it can be controlled defines another constraint on feature size. While the  $Y$  and  $Z$  positioning of the focal point are addressable with sub-micron accuracy via analogue control of the galvanometer mirror and the objective-lens scanner, respectively, the continuous sinusoidal motion of the resonant scanline along the  $X$ -axis precludes direct control of feature size. Instead,  $X$ -axis voxel positions and sizes are defined by the rate at which the laser beam power can be modulated across the polymerisation threshold. Given the Pockels cell update frequency and the resonant scanner sweep rate, the  $X$ -axis resolution should be  $\sim 2.5\text{--}5.6 \mu\text{m}$  (at the edge and centre of the resonant sweep, respectively) at  $1 \times$  zoom, with minimum feature size decreasing linearly with increasing magnification—for example, the  $300\text{-}\mu\text{m}$  scale used for the resolution tests in Fig. 5 should have  $X$  voxel widths of  $\sim 1.1\text{--}2.5 \mu\text{m}$  (edge and centre, respectively). In Section 3.3 we report results for worst-case resolution—those voxels at the centre of the  $X$  sweep.

#### 2.4.2. Two-photon polymerisation

The minimum feature resolution of a two-photon polymerisation process is a nonlinear function of the precision of laser focal point

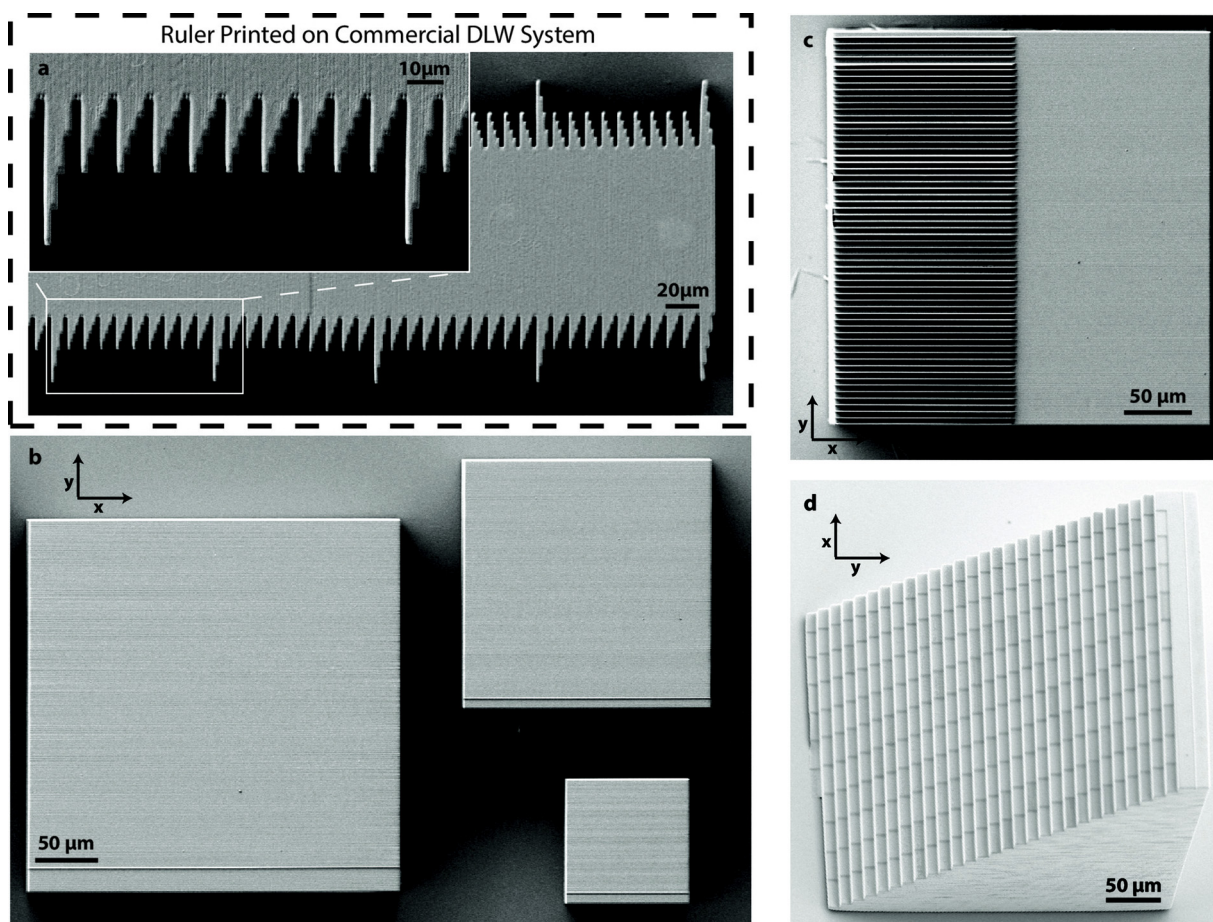


**Fig. 2.** Rulers for calibrating the rDLW system. (a) Ruler for measuring X- and Y-workspace dimensions. (b) Cubes used to calibrate object size and uniformity of power delivery. The cubes shown have widths 300, 200, and 100  $\mu\text{m}$ . The printing parameters were  $2.2\times$  (i.e.,  $302 \times 302 \mu\text{m}$  FOV),  $3.3\times$  and  $6.6\times$  magnification (zoom), respectively. Each X–Y plane was built with  $152 \times 1024$  voxels, and the vertical spacing between the planes was  $0.5 \mu\text{m}$  for all three cubes. (c) Ruler for Y-axis calibration. The printing parameters are the same as for the 300- $\mu\text{m}$  cube in (b). The horizontal line spacing on the ruler is  $5 \mu\text{m}$ . (d) Vertical ruler for Z-axis calibration. Each row along the X axis contains 11 steps with  $1\text{-}\mu\text{m}$  height difference. Adjacent steps along the Y axis have  $10\text{-}\mu\text{m}$  height difference. The total height of the ruler is  $300 \mu\text{m}$ . The printing parameters were the same as for the 300- $\mu\text{m}$  cube in (b).

control, laser power, and the chemical kinetics of the photoresist [26]. This complexity makes it challenging to predict the effective printing resolution of any DLW system, and thus each hardware configuration and photoresist combination must be verified experimentally.

The dimensions of the laser's focal point constrain minimum feature size, as they define the region in which photon density is sufficiently high to initiate the polymerising reaction. The focal point's radial (i.e., along the X- and Y-axes) and axial (along the Z-axis) dimensions are functions of the laser's wavelength,  $\lambda$ , and the numerical aperture, NA, of the objective lens. Assuming an ideal Gaussian beam profile, the full-width half-maximum size of the point spread function is  $\lambda/(2 \cdot \text{NA})$  (radial) and  $\lambda/(2 \cdot \text{NA}^2)$  (axial) [27]. With our operating laser wavelength (780 nm) and objective lens NA (0.8), these dimensions are 488 and 609 nm, respectively. Other factors may affect the size of the focal point—for example, if the laser beam incompletely fills the back of the objective, the effective NA will be lower, whereas changing the laser's power will control the portion of the point spread function that crosses the polymerisation threshold [28].

Resolution results may be found in Section 3.3.

### 2.5. Energy deposition

Given sinusoidally varying scan velocity (Fig. 3a, Section 2.4.1) and constant laser power at the focal point, the photoresist experiences different light exposure conditions as the beam accelerates from the

start of a raster line until it reaches peak velocity at the centre of the sweep and then decelerates as it approaches the end of a line. Under these conditions, the photoresist will not polymerise evenly, and may vapourise or boil where the beam's speed is low. Thus the baseline power of the polymerising laser must be corrected for the focal point's speed—a factor of  $\cos(t) = \cos(\arcsin x)$ —in order to maintain constant exposure.

Another source of variability in the laser energy available for polymerisation is attenuation of the beam due to inhomogeneities in laser intensity over the workspace. This may be due to vignetting, which attenuates laser power toward the edges of the workspace, or to other effects such as those resulting from imperfect alignment of optical components. Falloff due to vignetting is complex, depending on the angles at which the laser enters and exits each lens in the system, relative alignments of all optical components, the shape of the laser beam, partial occlusions throughout the optical path, and, in general, attenuation of the light, although this should be negligible in the near field of a laser. Furthermore, some of these factors may change frequently on a multipurpose tool in a research environment.

Due to the difficulty of modelling these factors precisely, we use a simple adaptive approach to compensate for nonuniform optical fields. Given a model  $M = f: x, y \rightarrow \text{falloff}$ , we boost power by  $1/M$  to compensate.

The photoresist used in these assays (IP-Dip) fluoresces when exposed to 390-nm light (i.e., two near-simultaneous 780-nm photons) at

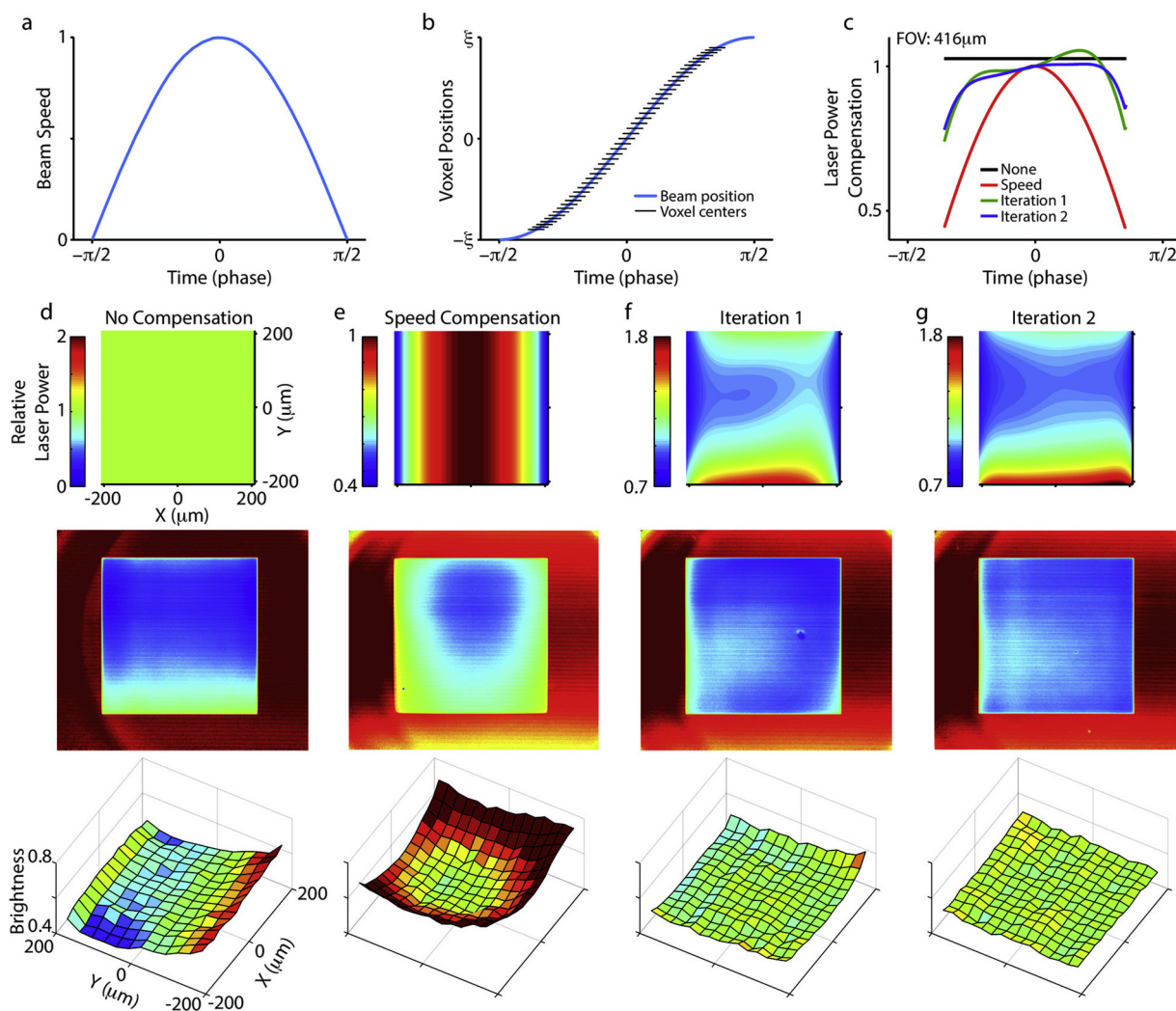


**Fig. 3.** Sinusoidal laser velocity over the X-axis results in nonuniform voxel size. Both that and optical nonuniformities such as vignetting require corrective laser power compensation. (a) Laser focal point velocity as the resonant scanner sweeps across the X-axis. (b) Laser focus position varies sinusoidally with time (blue line). The active scanning region is restricted to a portion  $D$  of the sweep, with X-axis voxel positions shown as black horizontal dashes. For clarity, we show where voxels would be defined for an 8-kHz resonant scanner with a 1-MHz control system, which yields only 45 voxels. In order to maintain uniform energy deposition across the workspace, laser power is modulated by two factors: it is scaled along the X-axis by the focal point's speed  $\cos(t)$ , and along the X-Y plane by a learned model of the inverse of optical darkening due to polymerisation. (c) Cross-section of the power compensation along X, in which  $y = 0$ ,  $x \in [-208, 208] \mu\text{m}$  ( $1.6 \times$  zoom on our rDLW system). (d–g)  $400 \times 400 \times 100\text{-}\mu\text{m}$  bricks used to measure and calibrate energy deposition. The upper image shows the print power mask over the  $208 \times 208\text{-}\mu\text{m}$  workspace; the middle image shows an actual printed object (normalised using a baseline fluorescence image); and the bottom image shows brightness data gathered by sweeping the object over the lens so that the same set of pixels in the imaging system may be used for each measurement in order to bypass optical nonuniformities therein. Shown: (d) constant power (note that (1) at this zoom optical vignetting comes close to compensating for X-axis nonuniformity due to varying beam speed; and (2) this image was printed at lower nominal power than the others in order to avoid boiling); for the other images, the speed compensation appropriately reduces power); (e) only (X-sinusoidal) speed power compensation; (f,g) two iterations of adaptive power compensation over the visual field (see Section 2.5). The images and data were obtained with ScanImage on our rDLW system. (For interpretation of the references to colour in this figure legend, the reader is referred to the web version of this article.)

an intensity far lower than that required for polymerisation. Polymerised resist fluoresces less brightly, approximately proportional to the degree of polymerisation. Thus  $M$  may be approximated by measuring the reduction in fluorescence of polymerised photoresist over a printed object.

In order to calibrate the energy deposition curve, we printed  $400 \times 400 \times 100\text{-}\mu\text{m}$  solid bricks and estimated the uniformity of polymerisation by measuring the fluorescent intensity of the bricks at a depth of  $3 \mu\text{m}$  below their top surfaces, immediately after printing the test objects (without removing them from the printer), using the ScanImage software at  $1 \times$  zoom. To eliminate the effects of spatial nonuniformity (such as vignetting) in our imaging system, rather than photographing still images and measuring brightness values over the imaging plane, we instead moved the printed objects under the lens (at

$200 \mu\text{m/s}$  along the X-axis) using a motorised nanopositioning stage and recorded over time (at  $15.21 \text{ Hz}$ ) the brightness values over the 1-pixel-by- $10\text{-}\mu\text{m}$  XY region of the printed cube at the centre of the camera's reference frame at each X-axis step. This was repeated for 15 equally spaced lines covering the Y axis. A control image of the field of view without any objects was captured, and intensity values of the images of each test object were divided by the control image's intensity in order to normalise image brightness.

From these data we fit a curve such that falloff at any point may be interpolated (in Fig. 3 we use fourth-order polynomials in X and Y, although other functions may be suitable). Due to the nonlinear relationships between applied laser power and degree of polymerisation [29,30] and between degree of polymerisation and reduced fluorescence of the polymerised photoresist, this will not yield a perfect

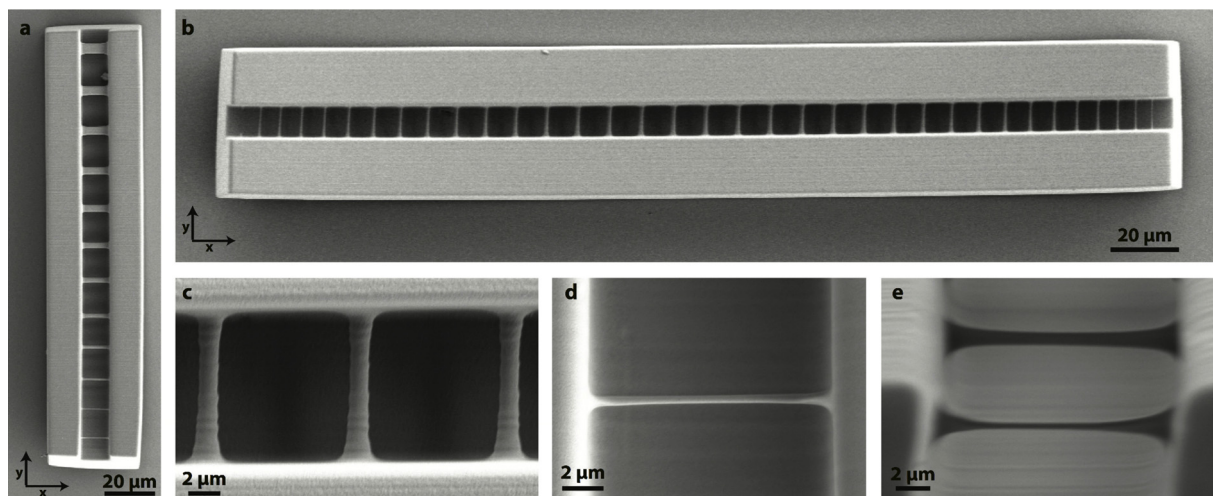


**Fig. 5.** Objects with one- and two-voxel features printed on our rDLW system. (a) Object used to estimate minimum voxel size on the Y and Z-axes. All bridges have single-voxel height (Z), and increasing width on the Y-axis. The bottom bridge has one-voxel width; thus, it gives an idea of the thinnest suspended structure that can be achieved with the parameters and photoresist used here. The object was printed with  $2.2\times$  magnification for a  $302 \times 302 \mu\text{m}$  field of view. The resolution of each focal plane is  $152 \times 1024$  voxels. The vertical distance between Z planes in the support structure is  $0.5 \mu\text{m}$  (the bridges span only a single Z plane). (b) Object used to estimate the voxel size on the X-axis. The printing parameters are the same as in (a). The bridges were designed to be two voxels wide on the X-axis, so their size follows a sinusoidal distribution due to the cosinusoidal speed profile of the laser beam. (c) Top view of the central bridge of (b), which represents the largest value in the workspace of double-voxel X resolution at this zoom level. (d) Top view of the lowest bridge of (a). (e) View of the lowest bridge of (a) at  $60^\circ$  from the top view.

compensation model in one step, so the process is iterated until sufficiently uniform energy deposition is achieved. On our hardware, two iterations of the adaptive deposition calibration reliably yielded good results. An example of this iterative calibration procedure is shown in Fig. 3d–g.

These two forms of power compensation—for focal-point speed and for optical inhomogeneities—are important for uniform printing. Furthermore, they demonstrate that polymerisation may be arbitrarily controlled on a per-voxel basis throughout printed objects, potentially allowing for easy development of techniques that take advantage of nonuniform polymerisation.

## 2.6. Programming and analysis

All programming, modelling and analysis was done in MATLAB (The Mathworks, Framingham, MA) running under Windows 10 on a desktop computer with an Intel i7 processor and 16 GB of RAM.

## 2.7. Design of calibration objects and print models

All custom benchmarking and example objects described here were created with Solidworks2016 (Dassault Systèmes, Concord, MA) and exported using the native STL converter. Calibration objects not printed on our rDLW system (see Fig. 2a) were printed using a Nanoscribe Photonic Professional GT (Nanoscribe GmbH, Stutensee, Germany). STL files for the Darwin Bust (Fig. 1d) and Torus Knot (Fig. 4c) were obtained from the Museum of Applied Arts and Sciences in Sydney, Australia and Tadej Skofic, respectively.

## 2.8. Scanning electron microscopy

Measurements of printed objects were made using SEM micrographs. To enhance sample conductivity, the samples were sputter-coated with gold (Sputter Coater 108) prior to imaging. The samples were placed 3 cm under the gold target and were coated for 1 min at 0.05 mbar and 20 mA. SEM imaging was performed with a Zeiss Supra 55VP Field Emission SEM. The samples were imaged at 6-mm working distance with the secondary electron sensor, 3-kV accelerating voltage and  $30\text{-}\mu\text{m}$  aperture size.

## 2.9. Photoresists and post-processing

A key step in developing a DLW solution is identifying photoresists that are compatible with both the specifications of the printing process (e.g., two-photon polymerisation, laser wavelength and power output, printing speed, etc.) and the requirements of the application (e.g., hardness, adhesion, biocompatibility, optical clarity, etc.). Though multiple photoresist formulations have been described, the majority used for two-photon DLW consist of soluble organic monomers or oligomers (typically acrylate derivatives) that are cross-linked, and thus made insoluble, by free radicals or cations produced by the exposure of a photoinitiator or photoacid generator [31]. The use of a tunable laser in the described rDLW system offers the possibility of printing with a variety of commercially available, custom, or proprietary photoresists.

In an effort to ensure that our assays were representative of the limits of our rDLW system's performance, all benchmark measurements were performed on objects printed with a high-performance photoresist, IP-Dip (Nanoscribe GmbH, Stutensee, Germany). IP-Dip is a proprietary liquid photoresist that is refractive-index-matched to glass to minimise optical distortion and enable rapid, fine-resolution two-photon polymerisation. IP-Dip polymerises under 390-nm light (i.e., the two-photon effective wavelength of our 780-nm source), producing solid, semi-transparent acrylic objects that have been used in biomedical, optical, and microfluidic applications.

To demonstrate the generalisability of our system, we printed objects in a commercial hybrid polymer photoresist based on Ormocomp (Microresist Technology GmbH, Berlin, Germany). Like IP-dip, Ormocomp polymerises under 390-nm light to producing solid, transparent structures for optical and microfluidic applications. Due to its high polymerisation threshold and the very high line scan speeds used in rDLW, additional photoinitiators were required to maintain high print resolution. For the example shown in Fig. 1d, standard Ormocomp was mixed with 1% by weight photoinitiator ((2,4,6-trimethylbenzoyl) phosphine oxide, TPO). Fluorescein salt dissolved in methanol ( $0.5 \mu\text{g}/\text{mL}$ ) was added to improve visualisation of the printing process.

Following printing, residual un-polymerised resist was removed by submerging the build plate and printed object in either propylene glycol methyl ether acetate (for IP-Dip) or OrmoDev (for Ormocomp-based hybrid) for 20 min. The prints were subsequently rinsed in methoxy-nonafluorobutane (3M Novec 7100 Engineering Fluid) to remove trace

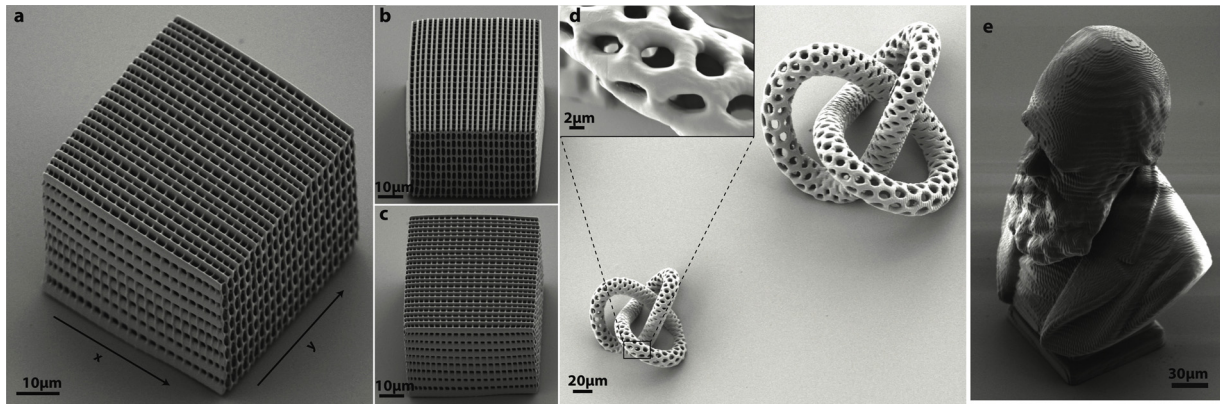


**Fig. 4.** Complex geometric objects printed with our rDLW printer. (a–c) Woodpile structure with design dimensions  $60 \times 60 \times 60 \mu\text{m}$ . Along the X-axis, bar thickness was 2 voxels ( $0.8 \mu\text{m}$ ) and bar spacing 4 voxels ( $1.6 \mu\text{m}$ ). Bar thickness and spacing on the Y-axis were 13 and 26 voxels respectively in order to be the same size as the X-axis beams, and on the Z-axis bars are 1 voxel thick with  $6\text{-}\mu\text{m}$  spacing. The focal plane resolution was  $152 \times 1024$  voxels, and the focal plane (Z) spacing was  $0.2 \mu\text{m}$ . (d) A torus knot design printed at  $100 \times 100 \times 150 \mu\text{m}$  (top right) and  $50 \times 50 \times 75 \mu\text{m}$  (bottom left). The inset shows details within the circumscribed region of the bottom left structure. Both knots were printed with focal plane resolution  $152 \times 512$  voxels and focal plane spacing  $0.2 \mu\text{m}$ . (e) SEM micrograph of a Charles Darwin statuette printed with our rDLW printer.

solvent residue.

### 3. Results

#### 3.1. Speed

A key aim for our rDLW design was to increase fabrication speed through the introduction of a resonant scanner. As a first approximation, fabrication time is governed by two parameters: the speed with which the beam moves through the resist and the linear distance that the beam must traverse [9]. DLW systems typically use some combination of stage-based (i.e., using motorised stages to move the printed object relative to a stationary laser focus) and mirror-based (i.e., using mirrors to move the laser focus relative to a objective's stationary object) methods for polymerising the desired location. Each has its advantages, making direct comparisons challenging, but mirror-based scanning is capable of realising significantly higher scanning speeds while maintaining micro- and nanoscale feature sizes (Table 1).

In a resonant-scanner-based system with a resonant frequency of  $F_r$ ,

**Table 1**

Representative DLW laser scanning speeds and nominal minimum feature sizes reported in recent literature. “Present work” indicates scan speed with the printer configured as described for the examples presented ( $1.6\times$  zoom yielding a  $416 \times 416\text{-}\mu\text{m}$  workspace, and printing during only the left-to-right sweep of the resonant scanner) and the maximum speed (bidirectional printing at  $1.3\times$  zoom). Minimum feature size and scan speed covary as described in the text.

Positioning mechanism	Scanning speed (mm/s)	Nominal feature size ( $\mu\text{m}$ )	Reference
Stepper motor stage	10	1	[32]
Piezo stage	0.03–0.09	0.28–1.5	[16]
	0.06	0.065	[33]
	10–30	1.5	[17]
Digital micromirror device (DMD)	0.5–5	0.5–1.6	[18]
Galvo-galvo mirror	0.005–0.2	0.085–1.5	[19]
	0.01	1.3	[20]
	7	0.78–1	[21]
	0.4–200	0.2–1.2	[22]
	21–103	0.086–0.43	[15]
	400	1–10	[23]
	7200	1	[34]
Rotating polygon-galvo mirror	7200	1	[34]
Resonant-galvo mirror	3300–8200	1–4	Present work

and useable workspace dimensions of  $2\xi D$  along the scanning dimension, the average beam speed is  $2\xi DF_r$ . For example, at  $1.6\times$  zoom, our system's useable workspace along the X-axis is approximately  $412 \mu\text{m}$ , resulting in an effective mean beam speed of  $3.3 \text{ m/s}$ . Note that this estimate assumes printing only in one direction of the laser scan (Fig. 1b); bi-directional printing effectively doubles beam speed, although any misalignment of the two scan directions leads to inferior results. Note also that decreasing magnification increases the distance that the beam travels while commensurately increasing beam speed, leaving print time unchanged.

For our rDLW system, we can estimate fabrication time for an object from the linear printing distance (i.e., length of a scan line  $2\xi D$  times the number of scan lines per layer  $S_y$  times the number of layers  $S_z$ ) times the mean beam speed. For the large block in Fig. 2b, this results in an estimated fabrication time of  $\sim 22 \text{ s}$ , which comports well with our actual print time of  $\sim 25 \text{ s}$  (including some processing overhead). DLW systems vary widely and there are no established benchmarks, making general comparisons of writing speed and printing time difficult [13,26]. However, galvanometer-based two-photon microscopes, upon which the fastest extant micron-scale 3D printers are based, are typically an order of magnitude slower than resonant-scan microscopes. For example, at  $512 \times 512$  imaging pixels, resonant-scan microscopes typically achieve 30-Hz frame rates while typical galvo-based systems achieve  $\sim 1\text{--}2\text{-Hz}$  frame rates at the same scan angle and resolution [35]. A pure galvanometer beam control system designed for calcium imaging might attain a beam speed of  $200 \text{ mm/s}$  [22]. Were such a system used to write the solid block in Fig. 2b, fabrication time would be  $\sim 3.8 \text{ min}$ .

Many DLW systems realise significant time savings by optimising the laser path such that travel distance is minimised. For printed objects with small fill ratios, this strategy can produce substantial improvements in fabrication speed. Other strategies, such as the core-and-shell printing process [36], can reduce fabrication time for objects with low surface-area/volume ratios at the cost of an additional processing step. Our approach achieves uniform fabrication times across fill ratios by using a resonant scanner to sweep the beam over every point in the printing workspace (Fig. 1b), maximising travel distance. Thus our estimate of print speed on a fast galvanometer-based printer is a worst-case estimate. Nonetheless, the high mean speed (Table 1) still allows a significant improvement in print time for many objects of interest.

As with the estimates of accuracy and resolution below, our estimates of printing speed are highly dependent on our choice of optical components, printing parameters, and photoresist. Significant improvements or diminishments in all assayed metrics can be realised

with a different choice of hardware, laser power, or row/layer density.

### 3.2. Accuracy

For  $300 \times 300\text{-}\mu\text{m}$  cubes printed at  $2.2\times$  zoom, we found the errors in the size of the cube to be  $-5.6 \pm 1.2\text{ }\mu\text{m}$  ( $-1.9 \pm 0.4\%$ ) on the  $X$ -axis and  $6.5 \pm 1.0\text{ }\mu\text{m}$  ( $2.2 \pm 0.33\%$ ) on the  $Y$ -axis ( $\pm x$  indicates SEM pixel size  $x/2$ ).

The  $Z$ -axis steps had a nominal height of  $10\text{ }\mu\text{m}$ , and an actual mean height of  $10.0316\text{ }\mu\text{m}$ —an error of  $\sim 0.32\%$ , well within the surface profiler's claimed accuracy of  $< 0.75\%$ .

Because all measurements were made following immersion of the printed objects in solvent to remove unpolymerised resist (Section 2.9), our estimates from SEM micrographs include some degree of post-processing-related object shrinkage. Achieving maximum printing accuracy—with this or any other DLW system—requires precise calibration of scaling and print power, high-precision components, and careful control of post-processing deformation. Disentangling the contribution of each to our accuracy estimates is beyond the scope of this work, and our accuracy results must be taken as indicative rather than definitive.

### 3.3. Resolution

We quantified real performance by printing objects with thin single-voxel features (Fig. 5a and b) and measuring feature dimensions using SEM micrographs. During polymerisation, the forming polymer tends to shrink due to both the emerging binding forces and polymerisation quenching from molecules present in the liquid solution. These effects are reduced when the forming polymer is attached to a solid object (e.g., a previously polymerised structure). We report the feature size as it is measured in features attached to a larger solid structure, but we also note the sizes of isolated features. Structures that consisted of channels containing single-voxel bridges were printed at  $2.2\times$  zoom (an FOV of  $302 \times 302\text{ }\mu\text{m}$ ). Because single- $X$ -voxel bridges often broke during postprocessing, we also report 2- $X$ -voxel-wide bridges. We estimated resolution by measuring the size of the bridges where they are attached to the supporting walls, and also estimated minimum size of suspended features—giving an idea of possible shrinkage—by measuring the bridges at their centres. In order to directly control the number of voxels, the printer was given voxel maps created by hand rather than from STL files.

Measurements are shown in Table 2. Discrepancies between theoretical and realised results are probably due to the nonzero size and anisotropic shape of the focal point, postprocessing deformation, and a possible difference between rise and fall response times of our Pockels system.

**Table 2**

Printing resolution estimates. Resolution was estimated from SEM micrographs of the single- and double-voxel (2X) bridges in the objects shown in Fig. 5. Measurements of attached features were made proximal to the wall of the support structure; isolated-feature sizes were measured at the bridge centres. "Voxel dimension" is defined by the cell sizes used for voxelisation. We list theoretical voxel dimension for the  $X$ -axis as two numbers: at the centre and edges of the resonant scanner's sweep, respectively. We report measurements of  $X$  feature size at the centre of the resonant sweep—the region of the workspace in which we expect the largest minimum feature sizes.

	Voxel dimension ( $\mu\text{m}$ )	Attached ( $\mu\text{m}$ )	Isolated ( $\mu\text{m}$ )
$X$	2.5/1.1	$1.09 \pm 0.14$	$0.3 \pm 0.14$
2X	5.0/2.2	$2.73 \pm 0.06$	$1.26 \pm 0.06$
$Y$	0.3	$1.25 \pm 0.03$	$0.35 \pm 0.03$
$Z$	0.5	$2.10 \pm 0.05$	$0.45 \pm 0.05$

## 4. Discussion

### 4.1. Improving resolution

The accuracy and resolution that we report here are sufficient for a variety of complex thin-feature structures, such as the  $60\text{-}\mu\text{m}$  woodpile shown in Fig. 4a–c and the hollow torus knot structure in Fig. 4d. However, further improvement is possible. As the  $X$ -axis voxel resolution is in part defined by the rate of laser power modulation, upgrading the Pockels cell and/or control hardware may produce a substantial reduction in feature size across the whole  $X$ -axis. Improvement in all axes could be achieved by reducing the focal point size (e.g., by increasing the objective lens aperture, flattening the beam profile, or reducing power [28]), or using photoresists with higher polymerisation thresholds or reduced spatial expansion factors.

### 4.2. Laser power

Though the rDLW system we report achieves a significant increase in printing speed over prior work, it is nevertheless dependent on the physical limits of using laser radiation to initiate a localised polymerisation reaction. As laser scanning speed increases, laser power must also increase to ensure that sufficient polymerisation energy is delivered to a voxel within the shorter period of time in which the laser focus is within it. The printing configuration described here, using a 10-W pump laser to produce a 600–1400 mW mode-locked beam (which, after traversing the optics, is further reduced to  $\sim 130\text{ mW}$  at the sample), can fully polymerise IP-Dip at the described speeds, but further increases in beam speed—for example, due to a lower-magnification objective lens or faster raster scanner—would require use of a more powerful laser.

### 4.3. Print speed and resolution

The other factor limiting print speed is the required output resolution on the  $X$ -axis, which is dictated by the laser power control system—the Pockels cell, amplifier, and control board. We have chosen to allow our laser's power to dictate our choice of maximum test object size and thus our claim of a  $400 \times 400\text{ }\mu\text{m}$  workspace and its corresponding resolution.

### 4.4. Applications with variable power

Because our rDLW printer exposes all process parameters, and indeed all control software, to the user, our system is easily adaptable to experiments with novel fabrication techniques that take advantage of the unique feature of voxel-by-voxel modulation of laser power. This fine-grained power control proved useful in compensating for nonuniform optical effects such as vignetting, and could further be used to take advantage of intermediate states of polymerisation and the material properties that so arise (i.e., refractive index, rigidity, or fluorescence) [6]. In addition, laser power is nonlinearly correlated with minimum feature resolution [28], so per-voxel power modulation could provide additional control of the sizes of different single-voxel features in a single print process.

### 4.5. Variable laser wavelength

The use of a tunable femtosecond laser adds significant cost to our system, and could be replaced by fixed-wavelength fibre-based femtosecond sources. However, since tunable femtosecond lasers are common components of two-photon microscopes, we suggest that this more flexible laser may open up new material choices for polymerisation at a range of wavelengths. We have demonstrated the capabilities of the system using IP-Dip, a proprietary refraction-index-matched photoresist designed for high-resolution two-photon polymerisation.

However, the wide tunable range of modern two-photon laser sources (for our laser, 700–1050 nm), or the ease with which another laser can be added to the beam path, makes possible printing with commercial or custom resists having significantly different absorption spectrum peaks. This capability would simplify fabricating compound structures composed of multiple photoresists, each with different mechanical or optical properties [37].

#### 4.6. Suspended and overhanging features

A limitation of existing DLW techniques—which not infrequently influences printed object design—is the need to add structural supports under suspended features, lest gravity and movement of the photoresist during printing displace the incomplete features before they are anchored to the body of the object being printed. An unexpected benefit of the rDLW system is that the high speed of printing allows, to some degree, the printing of unsupported, suspended features in viscous liquid photoresists (like IP-dip). In addition to streamlining object design, the ability to print without the need of support structure potentially enables the fabrication of previously unrealisable objects.

#### 4.7. Stitch printing to increase maximum object dimensions

Though the maximum print size of the described rDLW system ( $\sim 400 \times 400 \times 350 \mu\text{m}$ ) is suitable for many micron-scale applications, there are use cases (e.g., tissue culture scaffolding) that require larger object sizes while maintaining micron resolution. Several photoresists, including IP-Dip, Ormocer, and SU-8, allow newly polymerised material to bond directly onto previously polymerised material without mechanical defect. This allows an object to be built by stitching together several overlapping sections, each of which we refer to as a *metavoxel*. Additionally, whereas for a single metavoxel the zoom setting controls both X-axis resolution and maximum object size, stitching allows decoupling of these two parameters by printing a single piece as multiple smaller overlapping pieces at higher magnification. When stitching multiple metavoxels together, a stage with absolute linear accuracy on the order of the desired resolution is required. While a discussion of stitching is outside the scope of this paper, we note that, as of this writing, PrintImage allows stitching using either the microscopy stage or a commercial hexapod system, thus allowing fast printing of arbitrarily large objects, and it can easily be extended to use other hardware.

#### 4.8. Rotating mirror scanning

While resonant scanners have been previously used in 2D laser printing [38,39], a more common approach for raster-scan printing uses a multi-sided mirror rotating at constant speed to sweep the across the workspace [40]. Replacing the resonant scanner in our rDLW printer with such a raster-scan mirror would triple print speed by eliminating the flyback and near-zero-speed portions of the beam path. It would allow nearly linear beam speed, providing uniform voxel size and obviating sinusoidal power compensation. Though this would remove the resonant rDLW's capacity to increase print resolution without a concomitant reduction in printing speed (i.e., zoom printing), a similar effect may be achievable by incorporating a zoom lens. Conversely, a change in mirror rotation speed would allow changes in X-axis resolution without affecting workspace size.

## 5. Conclusion

We reported on rDLW: a 3D printer based on a standard two-photon microscope with a resonant raster scanner and our custom PrintImage control application. The rDLW system provides several key advantages over existing commercially available systems including high printing speeds, full access to fabrication parameters, and ease of extensibility.

Building on the widely-used open-source ScanImage microscopy package, this work provides a platform for future modifications and customisations.

## Author Contributions

TJG and JMT conceptualised the project and implemented the initial proof of concept. BWP wrote the software for controlling the print process and integrated it with existing ScanImage routines. TMO and JMT designed the microscope modifications to enable the new print process. CM developed test print objects, created calibration protocols, made all SEM micrographs, and performed quantitative testing. BWP, TMO, and CM jointly contributed to device and process refinement. TJG and TMO supervised the project. BWP, CM, and TMO drafted the manuscript with input from all other authors.

## Conflict of interest

Timothy J. Gardner is an employee of Neuralink Inc.

## Acknowledgments

We wish to thank Alice White (Boston University) for use of her Nanoscribe Photonic Professional GT 3D printing system and for sharing her expertise with microfabrication processes; Jacob Franklin (Vidrio Technologies) for his assistance with ScanImage; Tadej Skofic for designing the Torus Knot shown in Figure 4d; and Engin Kizilgun for designing the chess pawn shown in Figure 1d. We also wish to thank Alberto Cruz-Martin, Todd Blute, Ian Davison, Jeff Gavornik, and L. Nathan Perkins for their helpful comments on earlier drafts of this manuscript. Furthermore, we are grateful for the packages on the MATLAB File Exchange from Alex A (Mesh voxelisation), Eric Johnson (STL File Reader), Paul Mico (stlTools), and Teck Por Lim (Significant Figures). This research was supported by NIH grant R01NS089679 and a sponsored research agreement with GlaxoSmithKline.

## References

- [1] S. Maruo, O. Nakamura, S. Kawata, Three-dimensional microfabrication with two-photon-absorbed photopolymerization, *Opt. Lett.* 22 (1997) 132–134, <https://doi.org/10.1364/OL.22.000132>.
- [2] J.H. Atwater, P. Spinelli, E. Kosten, J. Parsons, C. Van Lare, J. Van De Groep, J. Garcia De Abajo, A. Polman, H.A. Atwater, Microphotonic parabolic light directors fabricated by two-photon lithography, *Appl. Phys. Lett.* 99 (2011) 39–42, <https://doi.org/10.1063/1.3648115>.
- [3] T. Buckmann, N. Stenger, M. Kadic, J. Kaschke, A. Frölich, T. Kennerknecht, C. Eberl, M. Thiel, M. Wegener, Tailored 3d mechanical metamaterials made by dip in direct-laser-writing optical lithography, *Adv. Mater.* 24 (2012) 2710–2714, <https://doi.org/10.1002/adma.201200584>.
- [4] B.H. Cumpston, S.P. Ananthavel, S. Barlow, D.L. Dyer, J.E. Ehrlich, L.L. Erskine, A.A. Heikal, S.M. Kuebler, I.Y.S. Lee, D. McCord-Maughon, J. Qin, H. Rockel, M. Rumi, X.-L. Wu, S.R. Marder, J.W. Perry, Two-photon polymerization initiators for three-dimensional optical data storage and microfabrication, *Nature* 398 (1999) 51–54, <https://doi.org/10.1038/17989>.
- [5] M. Farsari, B.N. Chichkov, Materials processing: two-photon fabrication, *Nat. Photon.* 3 (2009) 450–452, <https://doi.org/10.1038/nphoton.2009.131>.
- [6] T. Gissibl, S. Thiele, A. Herkommer, H. Giessen, Two-photon direct laser writing of ultracompact multi-lens objectives, *Nat. Photon.* 10 (2016) 554–560, <https://doi.org/10.1038/nphoton.2016.121>.
- [7] T. Gissibl, S. Thiele, A. Herkommer, H. Giessen, Sub-micrometre accurate free-form optics by three-dimensional printing on single-mode fibres, *Nat. Commun.* 7 (2016) 11763, <https://doi.org/10.1038/ncomms11763>.
- [8] M. Malinauskas, A. Žukauskas, V. Purlys, K. Belazaras, A. Momot, D. Paipulas, R. Gadonas, A. Piskarskas, H. Gilbergs, A.G. ciūtė, I. Sakellari, M. Farsari, S. Juodkazis, Femtosecond laser polymerization of hybrid/integrated micro-optical elements and their characterization, *J. Opt.* 12 (2010) 124010 <http://stacks.iop.org/2040-8986/12/i=12/a=124010>.
- [9] M. Malinauskas, M. Farsari, A. Piskarskas, S. Juodkazis, Ultrafast laser nanostructuring of photopolymers: a decade of advances, *Phys. Rep.* 533 (2013) 1–31, <https://doi.org/10.1016/j.physrep.2013.07.005>.
- [10] F. Niesler, Y. Tanguy, 3d printers for the fabrication of micro-optical elements, *Opt. Photon.* 11 (2016) 44–47, <https://doi.org/10.1002/opph.201600028>.
- [11] E. Kabouraki, K. Terzaki, V. Melissinaki, M. Manousidaki, M. Vamvakaki, M. Farsari, Direct fs laser writing of 3D nanostructures, *Direct fs LASER Writing of*

- 3D nanostructures, Springer, 2015, pp. 3–30, <https://doi.org/10.1007/978-3-319-12217-5>.
- [12] R.R. Gattass, E. Mazur, Femtosecond laser micromachining in transparent materials, *Nat. Photon.* 2 (2008) 219–225, <https://doi.org/10.1038/nphoton.2008.47>.
- [13] H.-B. Sun, S. Kawata, Two-photon photopolymerization and 3d lithographic microfabrication, *NMR 3D Analysis Photopolymerization*, Springer Berlin Heidelberg, Berlin, Heidelberg, 2004, pp. 169–273, <https://doi.org/10.1007/b94405>.
- [14] M.A. Skylar-Scott, M.-C. Liu, Y. Wu, M.F. Yanik, Multi-photon microfabrication of three-dimensional capillary-scale vascular networks, *Society of Photo-Optical Instrumentation Engineers (SPIE) Conference Series*, vol. 10115 (2017), <https://doi.org/10.1117/12.2253520>.
- [15] J. Gottmann, High speed and high precision fs-laser writing using a scanner with large numerical aperture, *J. Laser Micro/Nanoeng.* 4 (2009) 192–196, <https://doi.org/10.2961/jlmm.2009.03.0009>.
- [16] M. Straub, M. Gu, Near-infrared photonic crystals with higher-order bandgaps generated by two-photon photopolymerization, *Opt. Lett.* 27 (2002) 1824–1826, <https://doi.org/10.1364/OL.27.001824>.
- [17] A. Ovsianikov, A. Deiwick, S. Van Vlierberghe, P. Dubruel, L. Möller, G. Dräger, B. Chichkov, Laser fabrication of three-dimensional CAD scaffolds from photosensitive gelatin for applications in tissue engineering, *Biomacromolecules* 12 (2011) 851–858, <https://doi.org/10.1021/bm1015305>.
- [18] Q. Geng, D. Wang, P. Chen, S. Chen, Ultrafast multi-focus 3-d nano-fabrication based on two-photon polymerization, *Nat. Commun.* 10 (2019) 1–7, <https://doi.org/10.1038/s41467-019-10249-2>.
- [19] M. Thiel, J. Fischer, G. von Freymann, M. Wegener, Direct laser writing of three-dimensional submicron structures using a continuous-wave laser at 532 nm, *Appl. Phys. Lett.* 97 (2010) 221102, <https://doi.org/10.1063/1.3521464>.
- [20] S. Maruo, K. Ikuta, Three-dimensional microfabrication by use of single-photon-absorbed polymerization, *Appl. Phys. Lett.* 76 (2000) 2656–2658, <https://doi.org/10.1063/1.126742>.
- [21] M. Farsari, G. Filippidis, K. Sambani, T.S. Drakakis, C. Fotakis, Two-photon polymerization of an eosin y-sensitized acrylate composite, *J. Photochem. Photobiol. A: Chem.* 181 (2006) 132–135, <https://doi.org/10.1016/j.jphotochem.2005.11.025>.
- [22] K. Obata, A. El-Tamer, L. Koch, U. Hinze, B.N. Chichkov, High-aspect 3d two-photon polymerization structuring with widened objective working range (WOW-2pp), *Light: Sci. Appl.* 2 (2013) e116, <https://doi.org/10.1038/lsa.2013.72>.
- [23] M.A. Skylar-Scott, M.-C. Liu, Y. Wu, A. Dixit, M.F. Yanik, Guided homing of cells in multi-photon microfabricated bioscaffolds, *Adv. Healthc. Mater.* 5 (2016) 1233–1243, <https://doi.org/10.1002/adhm.201600082>.
- [24] T.A. Pologruto, B.L. Sabatini, K. Svoboda, Scanimage: flexible software for operating laser scanning microscopes, *BioMed. Eng. OnLine* 2 (2003) 13, <https://doi.org/10.1186/1475-925X-2-13>.
- [25] S. Khan, J.C. Brumberg, An inexpensive fluorescent graticule, *Microsc. Today* (2014) 26–27, <https://doi.org/10.1017/S1551929513001326>.
- [26] C.N. LaFratta, J.T. Fourkas, T. Baldacchini, R.A. Farrer, Multiphoton fabrication, *Angew. Chem. Int. Ed.* 46 (2007) 6238–6258, <https://doi.org/10.1002/anie.200603995>.
- [27] H. Urey, Spot size, depth-of-focus, and diffraction ring intensity formulas for truncated Gaussian beams, *Appl. Opt.* 43 (2004) 620–625, <https://doi.org/10.1364/AO.43.000620>.
- [28] S. Kawata, H.-B. Sun, T. Tanaka, K. Takada, Finer features for functional micro-devices, *Nature* 412 (2001) 697–698, <https://doi.org/10.1038/35089130>.
- [29] J.B. Mueller, J. Fischer, F. Mayer, M. Kadic, M. Wegener, Polymerization kinetics in three-dimensional direct laser writing, *Adv. Mater.* (2014) 6566–6571, <https://doi.org/10.1002/adma.201402366>.
- [30] H.-B. Sun, K. Takada, M.-S. Kim, K.-S. Lee, S. Kawata, Scaling laws of voxels in two-photon photopolymerization nanofabrication, *Appl. Phys. Lett.* 83 (2003) 1104–1106, <https://doi.org/10.1063/1.1599968>.
- [31] J. Fourkas, *Fundamentals of two-photon fabrication*, in: T. Baldacchini (Ed.), *Three-Dimensional Microfabrication Using Two-photon Polymerization: Fundamentals, Technology, and Applications*, Micro and Nano Technologies Series, William Andrew Publishing, 2015.
- [32] G. Kumi, C.O. Yanez, K.D. Belfield, J.T. Fourkas, High-speed multiphoton absorption polymerization: fabrication of microfluidic channels with arbitrary cross-sections and high aspect ratios, *Lab Chip* 10 (2010) 1057–1060, <https://doi.org/10.1039/B923377F>.
- [33] W. Haske, V. Chen, J. Hales, W. Dong, S. Barlow, S. Marder, J. Perry, 65 nm feature sizes using visible wavelength 3-d multiphoton lithography, *Opt. Express* 15 (2007) 3426–3436.
- [34] C. Rensch, S. Hell, M.v. Schickfus, S. Hunklinger, Laser scanner for direct writing lithography, *Appl. Opt.* 28 (1989) 3754–3758.
- [35] J. Jonkman, C.M. Brown, Any way you slice it – a comparison of confocal microscopy techniques, *J. Biomol. Techn.* 26 (2015) 54–65, <https://doi.org/10.7171/jbt.15-2602-003>.
- [36] M. Thiel, R.R. Reiner, F. Niesler, Y. Tanguy, Method for producing a three-dimensional structure, US Patent 20160114530 (2016). <https://www.google.com/patents/US20160114530>.
- [37] H. Zeng, P. Wasylczyk, C. Parmeggiani, D. Martella, M. Buresi, D.S. Wiersma, Light-Fueled Microscopic Walkers, *Adv. Mater.* 27 (2015) 3883–3887, <https://doi.org/10.1002/adma.201501446>.
- [38] M.J. Schermer, R.D. Dowd, Resonant scanner control system, US Patent 5121138 (1990). <https://www.google.com/patents/US5121138>.
- [39] K. Takeshi, Scanning device with resonant light deflector, EP Patent App. EP19,940, 111,183 (1995). <http://google.com/patents/EP0637885A1?cl=zh-cn>.
- [40] N. Takizawa, E. Kataoka, Laser beam printing device with mirror rotation speed controlled by origin sensor signal, US Patent 5,677,724 (1997). <https://www.google.com/patents/US5677724>.